SCIENTIFIC REPORTS

OPEN

SUBJECT AREAS:
SENSORS
ELECTROCATALYSIS
STRUCTURAL PROPERTIES
ENVIRONMENTAL MONITORING

Received
24 January 2013

Accepted
20 September 2013

Published
7 October 2013

Correspondence and requests for materials should be addressed to X.J.H. (xingjiuhuang@iim.ac.cn) or Q.X.L. (liqun@ustc.edu.cn)

Facet-dependent electrochemical properties of Co_3O_4 nanocrystals toward heavy metal ions

Xin-Yao Yu[1], Qiang-Qiang Meng[2], Tao Luo[1], Yong Jia[1], Bai Sun[1], Qun-Xiang Li[2], Jin-Huai Liu[1] & Xing-Jiu Huang[1]

[1]Research Center for Biomimetic Functional Materials and Sensing Devices, Institute of Intelligent Machines, Chinese Academy of Sciences, Hefei 230031, PR China, [2]Hefei National Laboratory for Physical Science at the Microscale, University of Science and Technology of China, Hefei, Anhui 230026, PR China.

We revealed an interesting facet-dependent electrochemical behavior toward heavy metal ions (HMIs) based on their adsorption behaviors. The (111) facet of Co_3O_4 nanoplates has better electrochemical sensing performance than that of the (001) facet of Co_3O_4 nanocubes. Adsorption measurements and density-functional theory (DFT) calculations reveals that adsorption of HMIs is responsible for the difference of electrochemical properties. Our combined experimental and theoretical studies provide a solid hint to explain the mechanism of electrochemical detection of HMIs using nanoscale metal oxides. Furthermore, this study not only suggests a promising new strategy for designing high performance electrochemical sensing interface through the selective synthesis of nanoscale materials exposed with different well-defined facets, but also provides a deep understanding for a more sensitive and selective electroanalysis at nanomaterials modified electrodes.

Aiming at a more sensitive electroanalysis, a variety of nanomaterials or nanocomposites modified electrodes were very often explored for electrochemical detection of very trace levels of toxic heavy metal ions (HMIs). Very recently, nanoscale metal oxides as novel modifiers have been reported in electrochemical detection of HMIs[1–5]. Compared with traditional modifiers such as noble metals and biomolecules, the electrodes fabricated with nanoscale metal oxides are easy to synthesize with low cost[1,3,5]. However, as is often claimed, increased currents and increased analytical sensitivity are simply reflections of an increased microscopic surface area and not electrocatalytic activity or any other nano-effects. That is, the mechanism of using nanoscale metal oxides in electrochemical sensing of HMIs has not been proposed by considering their insulating property. Therefore, the design and implementation of new experimental approach combined with theoretical studies are extremely needed.

For a crystalline nanoscale material, different facets may have different geometric and electronic structures, and exhibit different physical and chemical properties[6–8]. Much more attention has been given to investigate the facet effects on catalysts, photocatalysts, electrocatalysts, Li-ion battery, supercapacitors and so on[9–24]. Take Co_3O_4 nanoscale materials as an example; Li *et al.* investigated the facet effect of Co_3O_4 on catalytic property for methane combustion[10]. Xiao *et al.* reported that the exposed facets of Co_3O_4 nanocrystals are very important for Li^+ transport in Li-ion battery[12]. Although oriented Co_3O_4 nanostructures have attracted wide attention, the direct experimental detection of HMIs with controlled crystalline morphology and orientation remains a significant challenge- that is, the facet effect in electrochemical sensor especially detection of HMIs is not proposed. Further, till now nanoscale Co_3O_4 has not been used to examine the electrochemical sensing of HMIs. It should be also pointed out that plenary theoretical investigations are expected to help to get deeper insight into the crystal facet effect, but most reports on the crystal facet effect did not adequately combined first-principles theoretical studies at atomic level with the experimental results[13,14,17,19–21,24].

In this work, we report the facile synthesis of Co_3O_4 with two different shapes. Using this non-conductive nanomaterial-modified electrode, we try to demonstrate the facet-dependent electrochemical behaviour of Co_3O_4 nanocrystals toward HMIs by combining the adsorption measurements and the density-functional theory (DFT) calculations. It has been recognized that the (111) facet of Co_3O_4 nanoplates has better electrochemical sensing performance than that of the (001) facet of Co_3O_4 nanocubes. Adsorption measurements and DFT calculations reveal that adsorption of Pb(II) is responsible for the difference of electrochemical

properties. To the best of our knowledge, this is the first study to investigate the effect of facet on electrochemical sensing behaviour toward HMIs. Our combined experimental and theoretical studies provide a solid hint to explain the mechanism of electrochemical detection of HMIs using nanoscale metal oxides. This strategy may be extended to other electrochemical sensors based on nanoscale metal oxides.

Results

Two simple routes have been designed to fabricate Co_3O_4 nanocubes and nanoplates (Supporting Information, **Figure S1**). Co_3O_4 nanocubes were synthesized by a one-step hydrothermal method with $Co(CH_3COO)_2$ as the only reactant. The Co_3O_4 nanoplates were obtained by a solvothermal method in ethylene glycol (EG) followed by a calcination treatment in air. **Figure 1** shows the representative scanning electron microscopy (SEM), transmission electron microscopy (TEM) and high resolution TEM (HRTEM) images of Co_3O_4 nanoplates and nanocubes. The TEM and HRTEM images of Co_3O_4 nanocubes are presented in **Figure 1a and b**, respectively. As seen, the particle size of Co_3O_4 nanocubes is about 20 ~ 40 nm. HRTEM (**Figure 1b**) and corresponding selected area electron diffraction (SAED) pattern (Inset in **Figure 1b**) indicate that the lattice fringe is 0.28 nm and the nanocube is exposed with six (001) facets. A typical SEM image taken for Co_3O_4 nanoplates is shown in **Figure 1c**. The low magnification SEM and TEM images in **Figure S2** demonstrated the homogeneity of Co_3O_4 nanoplates. It is seen that most of the nanoplates display well-defined hexagonal shape. The width and the thickness of the plates is determined to be 700 ~ 900 nm and 50 ~ 60 nm, respectively. The HRTEM image in **Figure 1d** clearly shows that the spacing between lattice fringes with an angle of 60° is 0.28 nm, which is consistent with the $(\bar{2}02)$ and $(0\bar{2}2)$ planes of cubic Co_3O_4. And it is also confirmed by the SAED pattern (Inset in **Figure 1d**) revealing a single crystal structure. Thus, the resulting dominant exposed plates of Co_3O_4 nanoplates are (111) facets. Powder X-ray diffraction patterns (XRD) (Supporting Information, **Figure S3**) of both nanocubes and nanoplates have identical peaks, which can be perfectly indexed to that of cubic spinel Co_3O_4 (Joint Committee on Powder Diffraction Standards (JCPDS) card no. 42-1467). No impurities have been detected, indicating the formation of pure cobalt oxides. The crystal sizes were calculated according to Sherrer equation based on the (311) diffraction peak of XRD data. The crystal size of Co_3O_4 nanocubes was 32.5 nm, which was consistent with the TEM observation. However, the crystal size of Co_3O_4 nanoplates was calculated to be 21.3 nm, which may be due to its porous structure. The specific surface areas of Co_3O_4 nanocubes and nanoplates have been measured by the Brunauer–Emmett–Teller (BET) method (Supporting Information, **Figure S4**). The measured specific surface areas for Co_3O_4 nanocubes and nanoplates are 20 and 13 $m^2\ g^{-1}$, respectively.

In general, the obtaining of metal oxides requires a basic medium, and usually NaOH is employed for this purpose. However, in the fabrication of Co_3O_4 nanocubes, the hydrolysis of acetate anions from $Co(CH_3COO)_2$ becomes a good source of hydroxyl anions (Equation (1)). The O_2 dissolved in the deionized water is supposed to act as the main oxidant. Partial Co(II) is transformed into Co(III) and the coexistence of Co(II) and Co(III) under the ambient environment prefers the formation of Co_3O_4 (Equation (2)). The low amount of hydroxyl anions in the solution may promote the formation of Co_3O_4 nanocubes with (001) planes. Similar result has also been reported by Xiao et al[12].

$$CH_3COO^- + H_2O \rightarrow CH_3COOH + OH^- \qquad (1)$$

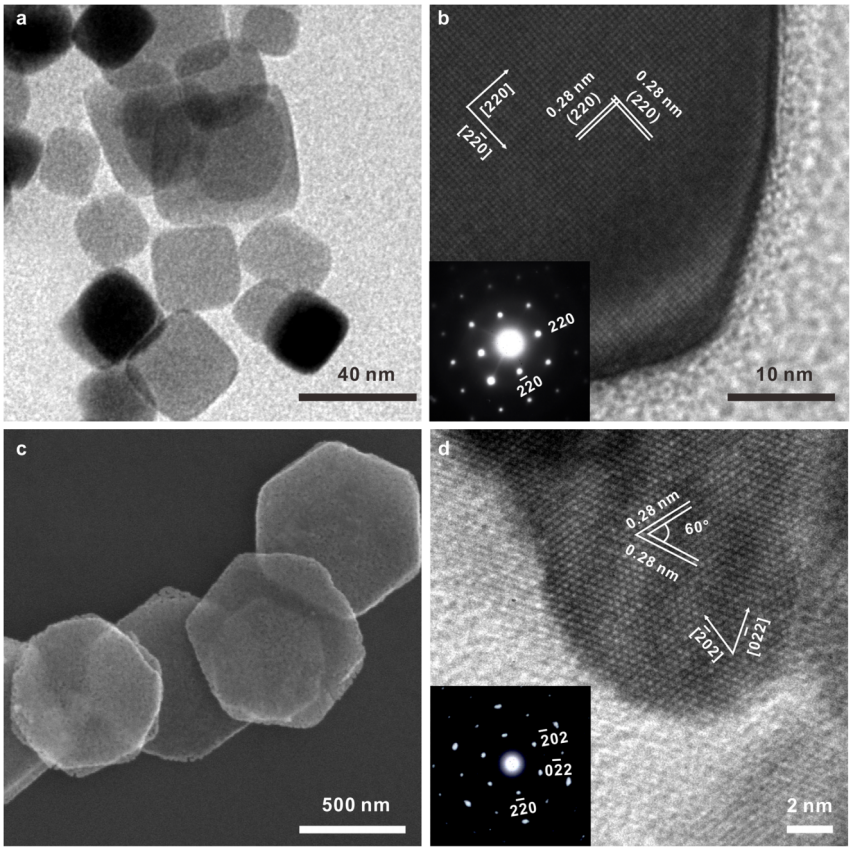

Figure 1 | Co_3O_4 nanocrystals. (a–b), TEM and HRTEM image of typical Co_3O_4 nanocubes. Inset in panel (b): SAED pattern of nanocubes. (c–d), SEM and HRTEM image of typical Co_3O_4 nanoplates. Inset in panel (d): SAED pattern of nanoplates.

$$6Co^{2+} + 12OH^- + O_2 \rightarrow 2Co_3O_4 + 6H_2O \quad (2)$$

From the SEM and TEM images of the Co_3O_4 nanoplates precursors before calcination (Data not shown), we can see that the plate-like structures of Co_3O_4 are inherited from these precursors. The typical XRD pattern of the precursors is shown (Supporting Information, **Figure S3**, black line). A strong diffraction peak around 10° in the XRD pattern is the characteristic of metal glycolates[25–28]. It has been assumed that EG would lose its two protons and the dianion complex with metal center[25]. Xia et al. has discussed the oligomerization process of metal glycolates. Longer chains of cobalt glycolate oligomers could self-assemble into ordered bundles (i.e., nanoplates) through van der Waals interactions and then precipitate out from the reaction medium[25]. After calcination, Co_3O_4 exposed mainly with (111) facets are obtained. However, the reason for the exposed (111) facets after calcination is not clear.

Co_3O_4 nanocubes and nanoplates modified glassy carbon electrodes (GCEs) are first electrochemically characterized by cyclic voltammetric (CV) and electrochemical impedance spectrum (EIS) (Supporting Information, **Figure S5**). As compared with the bare GCE, the anodic and cathodic peaks decrease at the Co_3O_4 modified electrode, which demonstrates that Co_3O_4 nanomaterials have been modified onto the surface of the GCE (Supporting Information, **Figure S5a**). It also indicates that the rate of electron transfer at the electrode surface is hindered with the attachment Co_3O_4 onto the GCE surface. In a typical Nyquist plot, the semicircle proton corresponding to the electron-transfer resistance (R_{et}) at higher frequency range while a linear part at lower frequency range represents the diffusion limited process[3]. The value corresponding to the bare GCE is about 27 Ω (Supporting Information, **Figure S5b**). And the value of Co_3O_4 nanocubes modified GCE (48 Ω) is comparable to that of Co_3O_4 nanoplates (50 Ω) (Supporting Information, **Figure S5b**). In this case, the surface area of the modified electrodes were calculated to be 0.0534 (nanoplates), 0.0519 (nanocubes), and 0.07065 (bare GCE) cm^2. This may be due to the insulating property of Co_3O_4 nanostructures, as such, the direct contribution of microscopic surface area could be avoided, which is very helpful to understand that the difference of electrochemical behavior is indeed from the effect of crystal facet (as will be discussed in the following).

Among all of the HMIs, lead has been identified as one of the most toxic heavy metals because of its detrimental effects on the human nervous system, blood circulation system, kidneys, and reproductive system[29]. Subsequently, the performances of these two types of Co_3O_4 with different exposed facets in electrochemical detection of heavy metal ions are comprehensively investigated. Pb(II) is used as a probe heavy metal ion. We first examined the square wave stripping voltammograms (SWASV) responses to Pb(II) in 0.1 M NaAc-HAc (pH = 5.0) at Co_3O_4 nanoplates and nanocubes modified electrodes (**Figure S6**). There is almost no obvious response at bare GCE, and at the meanwhile, a weak stripping response for nanocubes/GCE is observed. However, a strong and well-defined peak at −0.584 V is clearly seen for nanoplates modified GCE. And the peak current obtained is about 8 times and 13 times that of nanocubes/GCE and bare GCE, respectively. Moreover, the stripping peak shifts toward more positive potential and become progressively less symmetrical. This is the consequence of having more ions on the electrode (this is fully consistent with that more ions are adsorbed by nanoplates and release to the bare GCE, see Discussion section), and therefore requiring a longer sweep to remove the metal from the surface entirely. **Figure 2** shows that the current densities increase linearly versus the Pb(II) concentrations. For nanocubes/GCE, the linearization equation is $j/(\mu A\ cm^{-2}) = -122.9 + 174.4\ c/\mu M$. While for nanoplates/GCE, the linearization equation is $j/(\mu A\ cm^{-2}) = -131.1 + 372.7\ c/\mu M$. The results indicate that Co_3O_4 nanoplates with (111) facet exhibit better electrochemical detection performance than

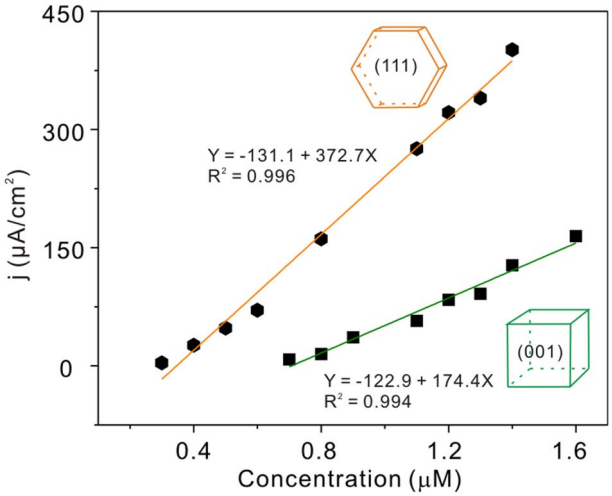

Figure 2 | Electrochemical properties of Co_3O_4 nanocrystals. Calibration plots of Co_3O_4 nanoplates and Co_3O_4 nanocubes modified electrode toward Pb(II) at different concentrations in 0.1 M NaAc-HAc solution (pH = 5.0). Considering the weak response at nanocubes modified electrode, the initial concentration is from 0.7 μM.

Co_3O_4 nanocubes with (001) facet. The sensitivity of Co_3O_4 nanoplates/GCE (372.7 $\mu A\ cm^{-2}/\mu M$) is over 2 times that of Co_3O_4 nanocubes/GCE (174.4 $\mu A\ cm^{-2}/\mu M$). The SWASV responses toward Pb(II) at various concentrations on Co_3O_4 nanoplates and nanocubes modified electrodes were seen in **Figure S7**. The limit of detection (LOD) as low as 0.12 nM and 0.16 nM (3σ method) for Co_3O_4 nanoplates and nanocubes, respectively was achieved. This meets the requirements of the World Health Organization (WHO) maximum permissible limit for lead concentration in drinking water of 10 $\mu g\ L^{-1}$. The LODs are better than existing methods based on noble metal and ion-imprinted polymers, such as gold nanofilm (0.1 μM)[30] and nano-sized Pb^{2+} imprinted polymer (0.6 nM)[31], etc. The LODs are also superior to some oxides, such as tube-in-tube SnO_2 (1.6 nM)[32] and SnO_2/graphene nanocomposites (0.18 nM)[33].

Discussion

We suggest that the difference in electrochemical behavior may have a relationship with the adsorption capacities of different nanoscale Co_3O_4 toward Pb(II). To confirm this contribution, the adsorption measurement is conducted in 0.1 M NaAc-HAc (pH = 5.0) in order to be consistent with electrochemical sensing conditions. Co_3O_4 nanocubes and nanoplates are incubated in Pb(II) solutions with different initial concentrations for 24 h to reach the adsorption equilibrium. The adsorption isotherms are shown in **Figure 3a and b**. Both the adsorption isotherms fit the Langmuir isotherm very well (Supporting Information, **Figure S8a** and **b**). The maximum adsorption capacity (q_{max}) of Co_3O_4 nanoplates (33.8 $mg\ g^{-1}$) is about 19 times that of Co_3O_4 nanocubes (1.8 $mg\ g^{-1}$). In previous result we have shown that Co_3O_4 is non-conductive material (Supporting Information, **Figure S5**). We believe that the higher adsorption performance of Co_3O_4 nanoplates than that of Co_3O_4 nanocubes lead to its better performance in electrochemical detection. It is important to emphasize that as the adsorption experiments were done in solution with dispersed Co_3O_4, while the Co_3O_4 were just coated onto the surface of the GCE, the electrochemical sensitivities for two types of Co_3O_4 would be not proportional to the adsorption capacities of them.

The above results and discussions experimentally show that Co_3O_4 nanocubes and nanoplates exhibit obviously different electrochemical sensing and adsorption performances. Co_3O_4 nanoplates with (111) planes exhibit larger sensitivity and adsorption capacity for heavy metal ions. Besides, we suggest that Pb(II) on the (111) facet are easier to diffuse onto GCE for reduction and

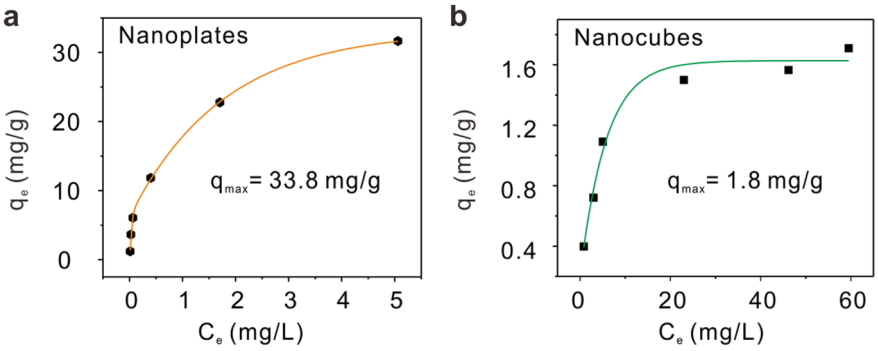

Figure 3 | **Adsorption measurements.** Adsorption isotherms of Pb(II) onto (a), Co_3O_4 nanoplates and (b), Co_3O_4 nanocubes.

stripping reaction than those on the (001) facet. Regarding the above surface area analysis of two kinds of Co_3O_4 (nanocubes > nanoplates), this further confirms that the differences in their electrochemical sensing performances are due to the facet effect.

To better understand the effect of facet on electrochemical behavior of Pb(II) on Co_3O_4 nanoplates and nanocubes, we perform DFT calculations to explore the adsorption and diffusion behaviors of Pb on Co_3O_4(001) and (111) surfaces. The adopted computational models are similar to the recent report on Li storage capability of Ti_3C_2 and $Ti_3C_2X_2$ (X = F, OH) monolayer[34]. The adsorption configurations of Pb atom on Co_3O_4(001) and (111) surfaces are optimized without any symmetry constraint. In the most energetically stable configuration of Pb/Co_3O_4(001) system, the Pb atom is four-coordinated by two oxygen and two Co surface atoms of Co_3O_4(001) surface (Supporting Information, **Figure S9**), and the Pb-O and Pb-Co bond lengths are 2.40 and 2.27 Å, respectively. For Pb/Co_3O_4(111) adsorption system, the Pb atom locates at the three-fold hollow site (Supporting Information, **Figure S10**), and the Pb-O bond length is 2.27 Å. Two corresponding adsorption configurations of Pb atom on Co_3O_4(001) and (111) surfaces are illustrated in top panel of **Figure 4** labeled with i and ii, respectively. The calculated adsorption energy of Pb atom on Co_3O_4(111) surface is −4.11 eV, which is larger than that on Co_3O_4(001) surface (−3.70 eV). The relative large adsorption energy for Pb/Co_3O_4(111) system mainly originates from the relative short Pb-O bond length. The Bader charge analysis[35] (Supporting Information, **Figure S11**) shows that the adsorbed Pb atom carries positive +0.36 and +0.10 |e| (e, the electron charge) on Co_3O_4(111) and (001) surfaces, respectively, which gives the quantitative proof of the relative strong Pb-substrate interaction for Pb/Co_3O_4(111) system. Note that there are four equivalent stable adsorption sites in a Co_3O_4(001) − $(\sqrt{2}\times\sqrt{2})$ cell and Co_3O_4(111) − (1 × 1) cell (Supporting Information, **Figure S9 and S10**), but the area of the former cell is larger than that of the latter one. In addition, the adsorption energy for Pb atom locating at the second stable adsorption site (labeled with II′ symbol within twelve cyan circles in Supporting Information, **Figure S10c**) on Co_3O_4(111) surface is predicted to be −3.81 eV, which is also larger than that of the most stable adsorption configuration of Pb/Co_3O_4(001) system. On the other hand, we have examined the full-coverage of Pb on the stable adsorption sites. The adsorption energy of each Pb on Co_3O_4(001) and (111) surfaces is predicted to be −3.38 and −3.69 eV, respectively. It is clear that they are consistent with the calculated results of low-coverage of Pb on Co_3O_4 facets. Thus, the Pb atom adsorption ability on Co_3O_4(111) surface is significantly larger than that on Co_3O_4(001) surface. Moreover, the high adsorption energies and the large charge transfer suggest that

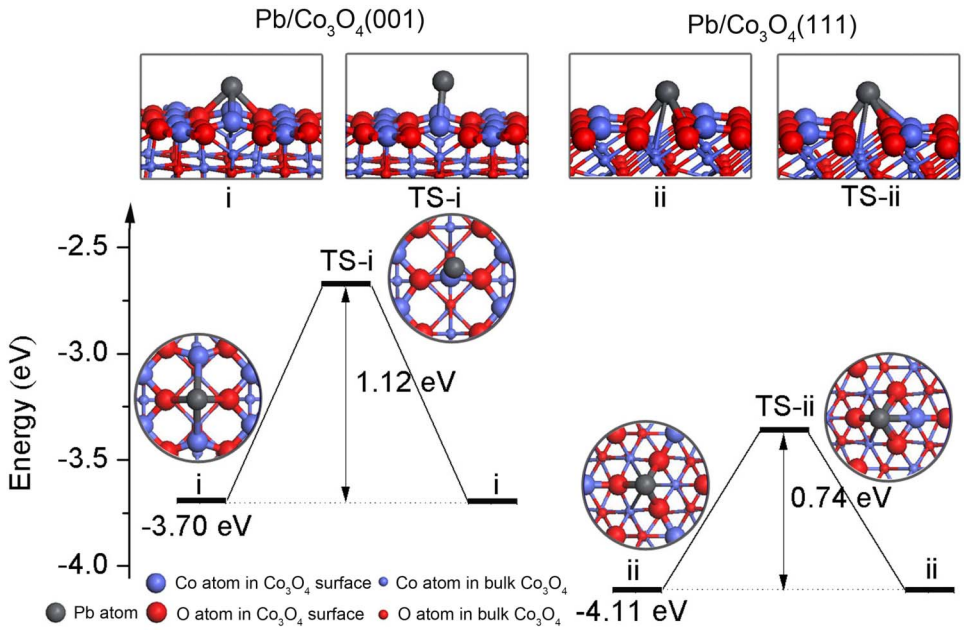

Figure 4 | **DFT calculations.** Top panel: side view of the optimized stable adsorption and transition-state (TS) structures for Pb on Co_3O_4(001) and (111) surfaces. Bottom panel: the TS barriers of Pb on Co_3O_4(001) and (111) surfaces, and top view of these optimized stable adsorption and TS structures are also shown. After overcoming the TS barriers, Pb reaches the nearest neighboring stable adsorption site.

the adsorbed Pb can form a strong Coulomb interaction with the Co_3O_4 surface.

Now we turn to calculate the energy barriers of Pb diffusing on Co_3O_4(001) and (111) surfaces using the climbing image nudged elastic band (CI-NEB) method[36]. The Pb has two diffusion paths from the most stable adsorption site to its nearest neighboring stable site on Co_3O_4(001) surface, while there are six diffusion directions for Pb/Co_3O_4(111) adsorption system (Supporting Information, **Figure S12**). The geometric structures of the transition-states for Pb on Co_3O_4(001) and (111) surfaces are shown in **Figure 4** labeled with TS-i and TS-ii, respectively. The calculated diffusion energy barrier of Pb on Co_3O_4(001) and (111) surfaces are predicted to be 1.12 and 0.74 eV, respectively. The relative low transition-state barrier results in the Pb fast diffusing on Co_3O_4(111) surface. These DFT results confirm that Co_3O_4(111) surface can capture more Pb than Co_3O_4(001) surface, and the adsorbed Pb diffuse more easily on the Co_3O_4(111) surface, consistent well with experimental observations.

Based on the above experimental and DFT calculated results, a schematic illustration of how adsorptive nanoscale materials with different exposed crystal facets could be designed for electrochemical sensing interface is depicted in **Figure 5**. As for bare GCE, there are not nanoscale materials which can effectively capture HMIs and the weaker stripping peak is obtained. Large amount of HMIs could be adsorbed onto the surface of nanoscale materials and then diffuse to the GCE surface. The more target HMIs are adsorbed onto the surface of nanoscale material, the more HMIs diffuse to the GCE and the stronger the stripping peak current obtains as a result. As Co_3O_4 nanoplates exposed with (111) facet can adsorb more metal ions than Co_3O_4 nanocubes with (001) facet and the metal ions on the surface of (111) facet can diffuse more easily onto the GCE, Co_3O_4 nanoplates modified GCE obtain larger stripping peak current. In contrast to previous studies[37–41] focusing on elevating the specific surface area of nanoscale materials in electrochemical sensing; our findings demonstrate that the construction of nanoscale materials onto electrode with well-defined exposed facets is crucial when considering the design of high-performance electrochemical sensor.

In summary, Co_3O_4 nanocubes and nanoplates have been successfully synthesized by facile methods by using different solvents. The predominantly exposed facets are (001) in the Co_3O_4 nanocubes and (111) in the Co_3O_4 nanoplates, respectively. Studies of their sensing properties revealed that the as-prepared Co_3O_4 nanocrystals exhibit interesting facet-dependent electrochemical behaviors toward HMIs based on their adsorption behaviors. The (111)-bound Co_3O_4 nanoplates are superior to (001)-bound Co_3O_4 nanocubes. Adsorption measurements revealed that Co_3O_4 (111) facets can adsorb more metal ions than the (001) facets. DFT calculations suggest that Co_3O_4(111) facets exhibit a relative larger adsorption energy, more adsorption sites, and a relative lower transition-state barrier than Co_3O_4(001) facets, which may be the predominant reason accounting for the facet-dependent electrochemical sensing behavior toward HMIs. Both adsorption experiments and DFT results agree well with the electrochemical sensing results. This study not only suggests a promising new strategy for designing high performance electrochemical sensing interface through the selective synthesis of nanoscale materials exposed with different well-defined facets, but also provides a deep understanding for a more sensitive and selective electroanalysis at nanomaterials modified electrodes.

Methods

Materials. All reagents were commercially available from Sinopharm Chemical Reagent Co., Ltd (China) with analytical grade. Stock solution used in electrochemical measurement of Pb(II) was prepared by dissolving $Pb(NO_3)_2$ in deionized water. 0.1 M acetate buffer (NaAc-HAc) solution of pH = 5.0 was prepared with NaAc and HAc. Ultrapure fresh water obtained from a Millipore water purification system (MilliQ, specific resistivity > 18 MΩ cm, S.A., Molsheim, France) are used in all runs.

Synthesis of Co_3O_4 nanocubes. 0.25 g of $Co(CH_3COO)_2 \cdot 4H_2O$ was loaded into a 23 mL poly(tetrafluoroethylene) (PTFE)-lined stainless steel autoclave, which was then filled with 18 mL water. The autoclave was sealed and maintained at 200°C for 12 h, and then cooled down to room temperature. The final products were centrifuged, rinsed with distilled water and ethanol for several times to remove any impurities.

Synthesis of Co_3O_4 nanoplates. 0.25 g of $Co(CH_3COO)_2 \cdot 4H_2O$ was loaded into a 23 mL poly(tetrafluoroethylene) (PTFE)-lined stainless steel autoclave, which was then filled with 18 mL ethylene glycol. The autoclave was sealed and maintained at 200°C for 12 h, and then cooled down to room temperature. The final products were centrifuged, rinsed with distilled water and ethanol several times to remove any impurities. The as-prepared precursors were finally calcined at 350°C in air for 3 h.

Characterization. The SEM images were taken by a FEI Quanta 200 FEG field emission scanning electron microscope. The TEM and HRTEM images analyses were carried out on a JEM-2010 microscope. XRD was performed on a D/MaxIIIA X-ray diffractometer (Rigaku Co., Japan), using Cu Kα (λKα1 = 1.5418 Å) as the radiation source. The nitrogen adsorption and desorption isotherms at 77 K were measured with a Micromeritics ASAP 2020 M analyzer. The Brunauer, Emmett, and Teller (BET) equation was used to obtain the specific surface areas. The Pb(II) concentrations were determined in the liquid phase using inductively coupled plasma atomic emission spectrometry (ICP-AES, Jarrell-Ash model ICAP 9000). Electrochemical experiments were recorded using a CHI 660D computer-controlled

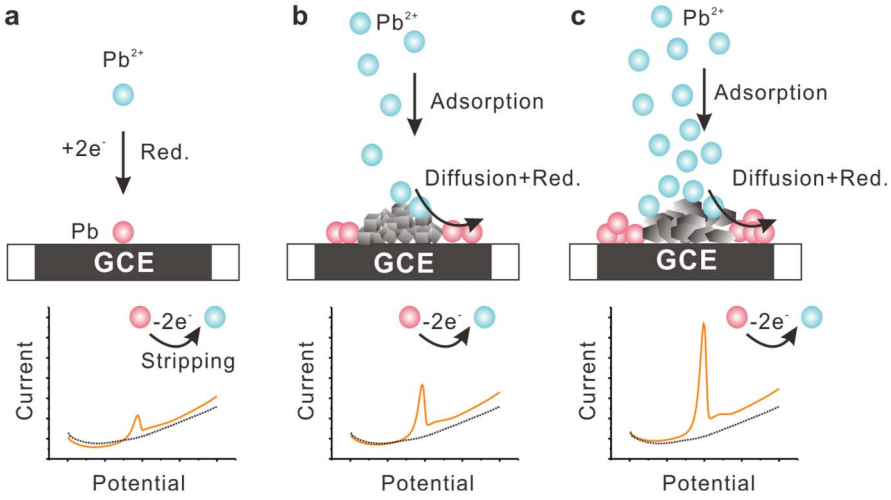

Figure 5 | Schematics of how adsorptive nanoscale materials exposed with different crystal facets could be designed to enhance the performance of electrochemical sensing. (a), Bare GCE. (b), Co_3O_4 nanocubes modified GCE. (c), Co_3O_4 nanoplates modified GCE. Facet-dependent electrochemical properties of Co_3O_4 nanocrystals toward heavy metal ions (e.g. Pb^{2+}) are investigated. The (111)-bound Co_3O_4 nanoplates are superior to (001)-bound Co_3O_4 nanocubes. Adsorption measurements reveal that Co_3O_4 (111) facet can adsorb more metal ions than the (001) facet. DFT calculations demonstrate that Pb on Co_3O_4(111) facet exhibits larger adsorption energies, more adsorption sites, and faster diffusion than on (001) facet.

potentiostat (ChenHua Instruments Co., Shanghai, China). A conventional three-electrode system consisted of a glassy carbon working electrode (GCE, 3 mm diameter), an Ag/AgCl as the reference electrode and a platinum wire as the counter electrode.

Fabrication of modified electrode. 2 mg of the as-prepared Co_3O_4 nanocubes and nanoplates were dispersed in 4 mL water with ultrasonic agitation to give a homogeneous solution. Prior to each modification, the bare GCE was sequentially polished with 1.0 μm and 0.05 μm alumina power slurries to a mirror shiny surface, and then sonicated with 1 : 1 HNO_3 solution, absolute ethanol and deionized water. The construction of Co_3O_4 on the surface of GCE was performed as follows: 5.0 μL of Co_3O_4 solution dripped onto the surface of a freshly polished GCE and then evaporating it at room temperature in the air.

Electrochemical measurements. The electrochemical measurement was carried out in SWASV mode for Pb(II) detection in 0.1 M NaAc-HAc solution. A deposition potential of −1.2 V was applied for 180 s to the working electrode under stirring. The SWASV responses were recorded between −1.0 to −0.2 V with step potential of 5 mV, amplitude of 20 mV, and frequency of 25 Hz. A desorption potential of 0 V for 210 s was performed to remove the residual metals under stirring condition.

Adsorption experiments. Experiments were carried out at 298 K in 10 mL polyethylene centrifuge tubes containing 1 $g \cdot L^{-1}$ adsorbent and various concentrations of Pb(II) for 24 h. The pH values of all these Pb(II) solutions 5.0 ± 0.2. After adsorption equilibrium, the adsorbent was separated by centrifugation. The Pb(II) concentrations remaining in the solution were analyzed. The amount of metal adsorbed (q_e) was calculated according to the following equation:

$$q_e = \frac{(C_0 - C_e)V}{m} \tag{3}$$

where C_0 and C_e represent the initial and equilibrium Pb(II) concentrations ($mg\ L^{-1}$), respectively, V is the volume of the solutions (mL), and m is the amount (mg) of adsorbent. A Langmuir isotherms model was used to analyze the experimental data. The mathematical expressions of the Langmuir isotherm is

$$\frac{C_e}{q_e} = \frac{1}{q_m K_L} + \frac{C_e}{q_m} \tag{4}$$

where q_m and K_L are Langmuir constants, representing the maximum adsorption capacity of adsorbents (mg/g) and the energy of adsorption, respectively. The values of q_m and K_L can be calculated from the slope and intercept of plots of $\frac{C_e}{q_e}$ versus C_e.

Computational methods. The DFT calculations were performed by using the Vienna ab-initio simulation package (VASP)[42,43] with the Perdew-Burke-Ernzerh parameterization of the generalized gradient approximation (GGA) adopted for the exchange correlation potential[44]. An energy cut of 400 eV were consistently used in our calculations. The atomic positions are fully relaxed with the conjugate gradient procedure until the residual forces vanished within 0.02 eV/Å. A 2 × 2 × 1 Monkhorst-Pack k-point was used to sample the surface Brillouin zone. Because Co_3O_4 is a strongly correlated antiferromagnet and Pb ion is one of HMIs, we also performed test DFT + U[45,46] (U = 3.3 eV and J = 0 eV according to previous reports[47]) calculations as well as PBE calculations with relativistic corrections[48] to Pb. As shown in **Table S1**, we can confirm that our PBE results are qualitatively correct. The transition states were obtained by using the climbing image nudged elastic band (CI-NEB) method[36].

Computational models. The optimized lattice constant (a_0) of the bulk Co_3O_4 is 8.12 Å, which is close to the experimental value (8.08 Å)[47]. The bulk Co_3O_4 shows antiferromagnetic properties. The 1 × 1 × 10 and 1 × 1 × 11 supercells were used to model the Co_3O_4 (001) and (111) surfaces, respectively, in which a 12 Å of vacuum is adopted. During the structural optimizations, we allowed the atoms in the top four layers in the supercells to relax fully, and fixed all other atoms in the bulk configuration. The side and top views of the optimized Co_3O_4 (001) and (111) surfaces are shown in **Figures S9** and **S10**, respectively. These optimized geometric structures agree well with the previous reports on the surface atoms arrangement of the Co_3O_4 nanocrystals with different crystal planes[10,47,49].

Adsorption energy. To compare the Pb adsorption ability on two different crystal planes, we define the Pb adsorption energy as $E_{ads} = E_{Pb/surface} - (E_{surface} + E_{Pb})$. Here, $E_{surface}$ and $E_{Pb/surface}$ are the total energies of the surface and the Pb atom adsorbing on surface, respectively, and E_{Pb} is the atomic energy of single isolated Pb atom. Under this definition, the more negative value stands for the more energetically stable adsorption.

Bader charge analysis and diffusion paths. To address the Pb-substrate interaction, we conduct the Bader charge analysis for Pb atom adsorbing on Co_3O_4 (111) and (001) surfaces. The corresponding results are presented in **Figure S11**. For clarity, the diffusion directions of Pb on Co_3O_4 (111) and (001) surfaces are illustrated in **Figure S12**.

1. Wu, Z. C. *et al.* Synthesis of mesoporous NiO nanosheet and its application on mercury(II) sensor. *J. Solid State Electrochem.* **16**, 3171–3177 (2012).
2. Wu, Z. *et al.* Synthesis of folding flake-like CuO sub-microstructure and its application on mercury(II) sensor. *J. Mater. Sci.: Mater. Electron.* **23**, 858–864 (2011).
3. Wei, Y. *et al.* High adsorptive γ-AlOOH(boehmite)@SiO_2/Fe_3O_4 porous magnetic microspheres for detection of toxic metal ions in drinking water. *Chem. Commun.* **47**, 11062–11064 (2011).
4. Yin, Z. J., Wu, J. J. & Yang, Z. S. A sensitive mercury(II) sensor based on CuO nanoshuttles/poly(thionine) modified glassy carbon electrode. *Microchim. Acta* **170**, 307–312 (2010).
5. Wei, Y. *et al.* Stripping voltammetry study of ultra-trace toxic metal ions on highly selectively adsorptive porous magnesium oxide nanoflowers. *Analyst* **137**, 2183–2191 (2012).
6. Jiang, Z. Y. *et al.* Syntheses and properties of micro/nanostructured crystallites with high-energy surfaces. *Adv. Funct. Mater.* **20**, 3634–3645 (2010).
7. Tao, A. R., Habas, S. & Yang, P. D. Shape control of colloidal metal nanocrystals. *Small* **4**, 310–325 (2008).
8. Jiang, L. *et al.* Synthesis of fivefold stellate polyhedral gold nanoparticles with {110}-facets via a seed-mediated growth method. *Small* **9**, 705–710 (2013).
9. Zhou, K. B. & Li, Y. D. Catalysis based on nanocrystals with well-defined facets. *Angew. Chem. Int. Ed.* **51**, 602–613 (2012).
10. Hu, L. H., Peng, Q. & Li, Y. D. Selective synthesis of Co_3O_4 nanocrystal with different shape and crystal plane effect on catalytic property for methane combustion. *J. Am. Chem. Soc.* **130**, 16136–16137 (2008).
11. Wang, Y. *et al.* Controllable synthesis of Co_3O_4 from nanosize to microsize with large-scale exposure of active crystal planes and their excellent rate capability in supercapacitors based on the crystal plane effect. *Nano Res.* **4**, 695–704 (2011).
12. Xiao, X. *et al.* Facile shape control of Co_3O_4 and the effect of the crystal plane on electrochemical performance. *Adv. Mater.* **24**, 5762–5766 (2012).
13. Huang, W. C. *et al.* Synthesis of Cu_2O nanocrystals from cubic to rhombic dodecahedral structures and their comparative photocatalytic activity. *J. Am. Chem. Soc.* **134**, 1261–1267 (2012).
14. Jin, M. S. *et al.* Shape-controlled synthesis of copper nanocrystals in an aqueous solution with glucose as a reducing agent and hexadecylamine as a capping agent. *Angew. Chem. Int. Ed.* **50**, 10560–10564 (2011).
15. Jin, M. S. *et al.* Palladium concave nanocubes with high-index facets and their enhanced catalytic properties. *Angew. Chem. Int. Ed.* **50**, 7850–7854 (2011).
16. Jun, Y. W., Choi, J. S. & Cheon, J. Shape control of semiconductor and metal oxide nanocrystals through nonhydrolytic colloidal routes. *Angew. Chem. Int. Ed.* **45**, 3414–3439 (2006).
17. Kim, D. *et al.* Convex polyhedral Au@Pd core-shell nanocrystals with high-index facets. *Angew. Chem. Int. Ed.* **51**, 159–163 (2012).
18. Kuo, C. H. *et al.* Facet-dependent and Au nanocrystal-enhanced electrical and photocatalytic properties of Au-Cu_2O core-shell heterostructures. *J. Am. Chem. Soc.* **133**, 1052–1057 (2011).
19. Li, Y. *et al.* Well shaped Mn_3O_4 nano-octahedra with anomalous magnetic behavior and enhanced photodecomposition properties. *Small* **7**, 475–483 (2011).
20. Wang, H. *et al.* Facet-dependent photocatalytic properties of AgBr nanocrystals. *Small* **8**, 2802–2806 (2012).
21. Wang, X. *et al.* Controlled synthesis and enhanced catalytic and gas-sensing properties of tin dioxide nanoparticles with exposed high-energy facets. *Chem.-Eur. J.* **18**, 2283–2289 (2012).
22. Wu, X. *et al.* Nanosized anatase TiO_2 single crystals with tunable exposed (001) facets for enhanced energy conversion efficiency of dye-sensitized solar cells. *Adv. Funct. Mater.* **21**, 4167–4172 (2011).
23. Zheng, Z. K. *et al.* Hierarchical TiO_2 microspheres: Synergetic effect of {001} and {101} facets for enhanced photocatalytic activity. *Chem.- Eur. J.* **17**, 15032–15038 (2011).
24. Zhou, X. M. *et al.* Facet-mediated photodegradation of organic dye over hematite architectures by visible light. *Angew. Chem. Int. Ed.* **51**, 178–182 (2012).
25. Jiang, X. C. *et al.* Ethylene glycol-mediated synthesis of metal oxide nanowires. *J. Mater. Chem.* **14**, 695–703 (2004).
26. Zhong, L. S. *et al.* 3D flowerlike ceria micro/nanocomposite structure and its application for water treatment and CO removal. *Chem. Mater.* **19**, 1648–1655 (2007).
27. Chakroune, N. *et al.* Synthesis, characterization and magnetic properties of disk-shaped particles of a cobalt alkoxide: $Co^{II}(C_2H_4O_2)$. *New J. Chem.* **29**, 355–361 (2005).
28. Larcher, D. *et al.* Some insights on the use of polyols-based metal alkoxides powders as precursors for tailored metal-oxides particles. *Chem. Mater.* **15**, 3543–3551 (2003).
29. Yu, X. Y. *et al.* Adsorption of lead(II) on O_2-plasma-oxidized multiwalled carbon nanotubes: Thermodynamics, kinetics, and desorption. *ACS Appl. Mater. Interfaces* **3**, 2585–2593 (2011).
30. Zhao, W. *et al.* Catalytic deposition of Pb on regenerated gold nanofilm surface and its application in selective determination of Pb^{2+}. *Langmuir* **23**, 8597–8601 (2007).
31. Alizadeh, T. & Amjadi, S. Preparation of nano-sized Pb^{2+} imprinted polymer and its application as the chemical interface of an electrochemical sensor for toxic lead determination in different real samples. *J. Hazard. Mater.* **190**, 451–459 (2011).
32. Chen, X. *et al.* SnO_2 tube-in-tube nanostructures: Cu@C nanocable templated synthesis and their mutual interferences between heavy metal ions revealed by stripping voltammetry. *Small* **9**, 2233–2239 (2013).

33. Wei, Y. *et al*. SnO_2/reduced graphene oxide nanocomposite for the simultaneous electrochemical detection of cadmium(II), lead(II), copper(II), and mercury(II): An interesting favorable mutual interference. *J. Phys. Chem. C* **116**, 1034–1041 (2012).
34. Tang, Q., Zhou, Z. & Shen, P. Are MXenes promising anode materials for Li ion batteries? Computational studies on electronic properties and Li storage capability of Ti_3C_2 and $Ti_3C_2X_2$ (X = F, OH) monolayer. *J. Am. Chem. Soc.* **134**, 16909–16916 (2012).
35. Sanville, E. *et al*. Improved grid-based algorithm for Bader charge allocation. *J. Comput. Chem.* **28**, 899–908 (2007).
36. Henkelman, G., Uberuaga, B. P. & Jonsson, H. *J. Chem. Phys.* **113**, 9901 (2000).
37. Hou, C. *et al*. Metal-organic framework templated synthesis of Co_3O_4 nanoparticles for direct glucose and H_2O_2 detection. *Analyst* **137**, 5803–5808 (2012).
38. Xu, J. *et al*. Facile synthesis of hierarchically porous Co_3O_4 nanowire arrays with enhanced electrochemical catalysis. *Electrochem. Commun.* **25**, 119–123 (2012).
39. Li, J. *et al*. High-sensitivity determination of lead and cadmium based on the Nafion-graphene composite film. *Anal. Chim. Acta* **649**, 196–201 (2009).
40. Ye, D. X. *et al*. Fabrication of Co_3O_4 nanoparticles-decorated graphene composite for determination of L-tryptophan. *Analyst* **137**, 2840–2845 (2012).
41. Li, Y. G., Tan, B. & Wu, Y. Y. Freestanding mesoporous quasi-single-crystalline Co_3O_4 nanowire arrays. *J. Am. Chem. Soc.* **128**, 14258–14259 (2006).
42. Kresse, G. & Hafner, J. Ab initio molecular dynamics for liquid metals. *Phys. Rev. B* **47**, 558–561 (1993).
43. Blochl, P. E. Projector augmented-wave method. *Phys. Rev. B* **50**, 17953–17979 (1994).
44. Perdew, J. P., Burke, K. & Ernzerhof, M. Generalized gradient approximation made simple. *Phys. Rev. Lett.* **77**, 3865–3868 (1996).
45. Anisimov, V. V., Zaanen, J. & Andersen, O. K. Band theory and Mott insulators: Hubbard U instead of Stoner I. *Phys. Rev. B* **44**, 943–954 (1991).
46. Anisimov, V. I., Aryasetiawan, F. & Lichtenstein, A. I. First-principles calculations of the electronic structure and spectra of strongly correlated systems: the LDA + U method. *J. Phys.: Condens. Matter* **9**, 767–808 (1997).
47. Montoya, A. & Haynes, B. S. Periodic density functional study of Co_3O_4 surfaces. *Chem. Phys. Lett.* **502**, 63–68 (2011).
48. Grabowski, B., Hickel, T. & Neugebauer, J. Ab initio study of the thermodynamic properties of nonmagnetic elementary fcc metals: Exchange-correlation-related error bars and chemical trends. *Phys. Rev. B* **76** (2007).
49. Xu, X.-L. *et al*. Bulk and surface properties of spinel Co_3O_4 by density functional calculations. *Surf. Sci.* **603**, 653–658 (2009).

Acknowledgement

This work was supported by the National Basic Research Program of China (2011CB933700, 2011CB921404, and 2014CB921101), the Natural Science Foundation of China (21073197, 21103198, 11205204, 11074235, and 11034006), and the China Postdoctoral Science Foundation (20110490386 and 2011M501073). X.J. H. acknowledges the One Hundred Person Project of the Chinese Academy of Sciences, China, for financial support.

Author contributions

X.J.H. conceived the electrochemical studies of nanocrystals with different facets. Q.X.L. designed the calculations. X.Y.Y. carried out all the experiments and Q.Q.M. performed calculation and contributed equally to this work. X.Y.Y. and Q.Q.M. co-wrote the paper. T.L., Y.J., B.S., and J.H.L. contributed data analysis and interpretation equally.

Additional information

Supplementary information accompanies this paper at http://www.nature.com/scientificreports

Competing financial interests: The authors declare no competing financial interests.

How to cite this article: Yu, X. *et al*. Facet-dependent electrochemical properties of Co_3O_4 nanocrystals toward heavy metal ions. *Sci. Rep.* **3**, 2886; DOI:10.1038/srep02886 (2013).